

Breaking the degeneracy between gas inflow and outflows with stellar metallicity: Insights on M 101

Xiaoyu Kang^{1,2,3*}, Ruixiang Chang⁴, Rolf-Peter Kudritzki^{5,6}, Xiaobo Gong^{1,2,3,7}
and Fenghui Zhang^{1,2,3}

¹*Yunnan Observatories, Chinese Academy of Sciences, 396 Yangfangwang, Guandu District, Kunming, 650216, P.R. China*

²*Key Laboratory for the Structure and Evolution of Celestial Objects, Chinese Academy of Sciences, 396 Yangfangwang, Guandu District, Kunming, 650216, P. R. China*

³*Center for Astronomical Mega-Science, Chinese Academy of Sciences, 20A Datun Road, Chaoyang District, Beijing, 100012, P. R. China*

⁴*Key Laboratory for Research in Galaxies and Cosmology, Shanghai Astronomical Observatory, Chinese Academy of Sciences, 80 Nandan Road, Shanghai, 200030, China*

⁵*LMU München, Universitätssternwarte, Scheinerstr. 1, 81679 München, Germany*

⁶*Institute for Astronomy, University of Hawaii, 2680 Woodlawn Drive, Honolulu, HI96822, USA*

⁷*University of Chinese Academy of Sciences, Beijing, 100049, P. R. China*

Accepted XXX. Received YYY; in original form ZZZ

ABSTRACT

An analytical chemical evolution model is constructed to investigate the radial distribution of gas-phase and stellar metallicity for star-forming galaxies. By means of the model, the gas-phase and stellar metallicity can be obtained from the stellar-to-gas mass ratio. Both the gas inflow and outflow processes play an important role in building the final gas-phase metallicity, and there exists degeneracy effect between the gas inflow and outflow rates for star-forming galaxies. On the other hand, stellar metallicity is more sensitive to the gas outflow rate than to the gas inflow rate, and this helps to break the parameter degeneracy for star-forming galaxies. We apply this analysis method to the nearby disc galaxy M 101 and adopting the classical χ^2 methodology to explore the influence of model parameters on the resulted metallicity. It can be found that the combination of gas-phase and stellar metallicity is indeed more effective for constraining the gas inflow and outflow rates. Our results also show that the model with relatively strong gas outflows but weak gas inflow describes the evolution of M 101 reasonably well.

Key words: galaxies: evolution – galaxies: abundances – galaxies: stellar content – galaxies: individual (M 101) – galaxies: spiral

1 INTRODUCTION

Chemical evolution modelling is a powerful tool to explore the galactic formation and evolution. Analytical chemical evolution models, based on simple parametrisation of key physical processes, such as gas accretion, star formation, nucleosynthesis, stellar mass return, and gas outflows, have been successfully employed to predict the enrichment of the interstellar medium (ISM) and achieved a series of interesting results. In the Milky Way, the closed-boxed chemical evolution model predicts a higher fraction of metal-poor G-dwarf stars in the solar neighborhood than observed (the classical "G-dwarf problem"), suggesting that the Milky Way disc is not a closed-boxed system and gas inflow is important for galactic evolution (Chang et al. 1999, and references therein).

The average chemical composition of the stars and the ISM can both provide constraints on the chemical enrichment history of galaxies. The gas-phase metallicity provides a snapshot of the metal content at a given time, while the mean stellar metallicity reflects the time-averaged value of the ISM metal content over the star formation history (SFH) of the galaxy. Most analytical chemical evolution studies in the literature focused on modelling gas-phase metallicity, since it is easier to measure than stellar metallicity in systems where individual stars cannot be resolved. Early analytical models derived a relation between gas-phase metallicity and the ratio of stellar to gas mass (Zahid et al. 2014; Yabe et al. 2015; Kudritzki et al. 2015). However, degeneracy among the model parameters (star formation efficiency (SFE, with the definition of the proportion of gas turns into stellar mass in unit time), the gas inflow and outflow rates (their definitions are in Section 2)), leads to severe limitations when using the gas-phase metallicity alone to con-

* E-mail: kxyysl@ynao.ac.cn

Table 1. Basic properties of M 101.

Property	Value
name	M 101, NGC 5457
RA	14 ^h 03 ^m 12 ^s .6
Dec	+54°20′57″
Morphology	Scd
Distance(adopted)	7.4 Mpc
Inclination	18°
R_{25}	25.81 kpc
Scale	36 pc arcsec ⁻¹

strain the model (Kudritzki et al. 2015; Belfiore et al. 2016). Better constraints can be obtained if both the stellar and the gas-phase metallicity are used at the same time. Fortunately, as demonstrated, for instance, by Zahid et al. (2017), the stellar metallicity of star-forming galaxies can be obtained from a population synthesis analysis of spectra of integrated stellar populations. Large samples of galaxies observed with spatially resolved spectroscopy are becoming available through recent integral field unit (IFU) surveys like CALIFA (Sánchez et al. 2012) and MaNGA (Bundy et al. 2015). Exploiting early data from such integral field spectroscopy surveys, Lian et al. (2018a,b) simultaneously explored the gas-phase and stellar metallicity, and pointed out that the stellar metallicity may contribute to breaking the degeneracy between parameters in analytical chemical evolution models.

To further investigate the importance of stellar metallicity in chemical evolution studies we take NGC 5457 (M 101) as an example and focus on its radial metallicity gradient. M 101 is a nearby face-on Scd galaxy (Freedman et al. 2001), which is known to be currently experiencing an inflow of high-velocity gas (Sancisi et al. 2008), and has likely been recently subjected to interaction events (Waller et al. 1997; Mihos et al. 2012). Its basic observational properties are summarized in Table 1, and their corresponding values are taken from Walter et al. (2008). Observations for gas-phase metallicity of HII regions along the disc of M 101 have been carried out since the 1970s (Searle 1971; Smith 1975; McCall et al. 1985; Kennicutt & Garnett 1996; Kennicutt et al. 2003; Bresolin 2007; Li et al. 2013; Croxall et al. 2016; Hu et al. 2018; Esteban et al. 2020). Croxall et al. (2016) carried out the most extensive study to date of oxygen abundance in M101, deriving a metallicity gradient with slope $-0.027 \pm 0.001 \text{ dex kpc}^{-1}$. Lin et al. (2013) derived the stellar metallicity gradient of M101, using spectral energy distribution (SED) fitting of ultraviolet, optical and infrared photometry. They found the stellar metallicity gradient to be flatter than that of HII regions. However, model explanation of these observed properties is still lacking.

The aim of this work is to investigate whether the analytical model introduced in Section 2 can explain the radial distributions of both gas-phase and stellar metallicity, and whether the stellar metallicity can help to relieve the degeneracy between gas inflow and outflows. The structure of this paper is as follows. The main ingredients of the model are described in Section 2. The observations are presented in Section 3. Our main results and discussion are shown in Section 4. The last section summarizes our main conclusions.

2 THE MODEL

Similar to our previous work (Chang et al. 1999; Kang et al. 2016, 2017), we assume that a star-forming galaxy is gradually built up due to continuous gas inflow. At the same time, outflows of metal enriched gas are also taken into account. We adopt the instantaneous recycling approximation (IRA) assuming that the gas return from stars to the ISM happens on a short timescale compared with galactic evolution, and we assume that the gas is well mixed with stellar ejecta. IRA represents a good approximation for oxygen produced by massive stars with short lifetimes. The chemical evolution of a galaxy is expressed by the classical set of integro-differential equations from Tinsley (1980):

$$\frac{dM_g}{dt} = \Phi - \Psi - (1 - R)\text{SFR}, \quad (1)$$

$$\frac{dM_*}{dt} = (1 - R)\text{SFR}, \quad (2)$$

$$\frac{d[Z_g \cdot M_g]}{dt} = y(1 - R)\text{SFR} - Z_g(1 - R)\text{SFR} + Z_i\Phi - Z_o\Psi, \quad (3)$$

where M_g and M_* are the gas mass and the stellar mass of the galaxy at evolution time t , respectively; Z_g is the gas-phase metallicity of the system. Φ and Ψ are the gas inflow rate and the gas outflow rate, respectively. SFR is the star formation rate (SFR). R is the return mass fraction and y is the nucleosynthesis yield. Both R and y depend on the adopted stellar initial mass function (IMF) but are only weakly dependent on metallicity and time (Vincenzo et al. 2016). The IMF of Kroupa et al. (1993) is adopted in this work, since this IMF is favored in describing the chemical evolution of the disc of spirals similar to the Milky Way (Vincenzo et al. 2016). Neither metallicity nor time dependence of R and y will be further taken into account in our model. The values of R and y are taken from Table 2 of Vincenzo et al. (2016) corresponding to the stellar yields of Romano et al. (2010). We obtain $R = 0.289$ and $y = 0.019$ from averaging the values of R and y_Z over metallicity, respectively. Z_i is the inflowing gas-phase metallicity. We adopted metal-free inflow, i.e., $Z_i = 0$. Z_o is the outflowing gas-phase metallicity and assumed to have the same metallicity as the ISM, i.e., $Z_o = Z_g$ (Chang et al. 2010; Kang et al. 2012, 2016, 2017).

Our model requires an assumption about matter inflow and outflows. Many chemical evolution models adopt an inflow rate of gas which follows an exponential law (Matteucci & Franco 1989; Hou et al. 2000; Spitoni et al. 2017, and references therein). An alternative, which we adopt for our model, is to assume that the gas inflow rate is proportional to the SFR, since the inflow of gas provides a continuous reservoir for star formation. Physical arguments in support of this assumption can be found in Matteucci & Chiosi (1983), Recchi et al. (2008), Bouché et al. (2010), Lilly et al. (2013) and Yabe et al. (2015). For the outflow rate we also assume that it is also proportional to the SFR because the larger is the SFR, the larger is the chance of having a larger-scale outflow (Silk 2003). With these assumptions analytical solutions of chemical evolution are straightforward (Recchi et al. 2008; Spitoni et al. 2010; Kudritzki et al. 2015). We use $\Phi = \omega(1 - R)\text{SFR}$, $\Psi = \lambda(1 - R)\text{SFR}$, where ω ($\omega \geq 0$) and λ ($\lambda \geq 0$) are the gas mass accretion factor and the outflow loading factor, respectively. ω and λ are two free parameters in our model. It should be pointed out that, under these assumptions, equation (1) combined with a linear star formation law from Schmidt (1959) (i.e., $\text{SFR} = \varepsilon M_{\text{gas}}$, ε is the so-called SFE in units of Gyr^{-1}) will lead to an exponentially

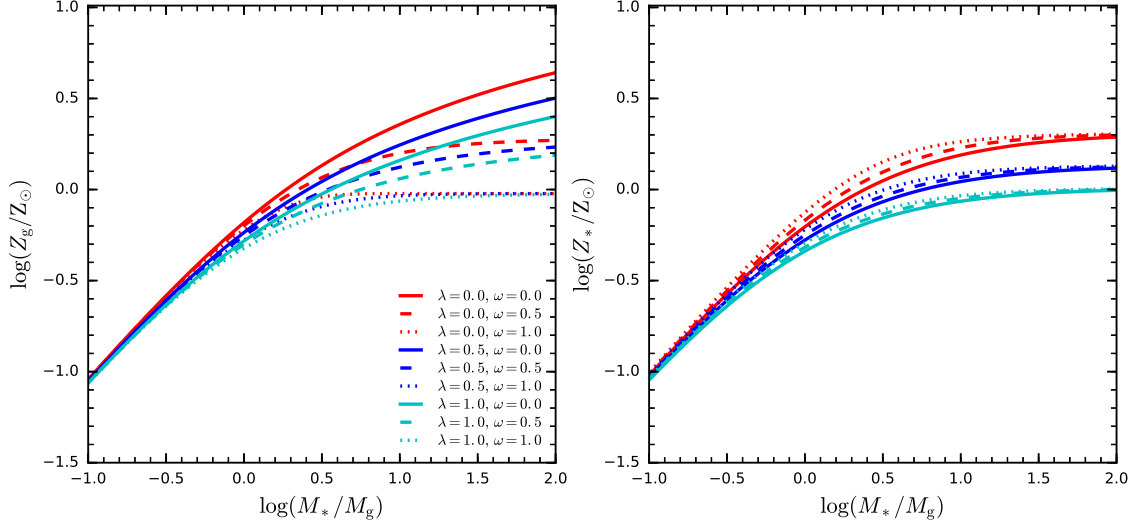


Figure 1. Metallicity as a function of the stellar-to-gas mass ratio with different combinations of gas outflow loading factor (λ) and gas mass accretion factor (ω). The lines with different color represent different values of λ , while the different line-types are corresponding to different values of ω . Gas-phase metallicity and stellar metallicity are displayed in the left panel and in the right panel, respectively.

declining SFR, that is, the inflow rate obeys the decaying exponential law, in agreement with the approach in [Matteucci & Francois \(1989\)](#).

With the definition $\alpha = \lambda - \omega$, equation (1) and (3) can be re-written as follows:

$$dM_g = -(1 + \alpha) \cdot dM_*, \quad (4)$$

$$d[Z_g \cdot M_g] = (y - Z_g - pZ_g) \cdot dM_*, \quad (5)$$

In this paper, we define the mean stellar metallicity as the mass-weighted average stellar metallicity,

$$\langle Z_* \rangle = \frac{(1 - R) \int_0^t Z_g(t') \text{SFR}(t') dt'}{(1 - R) \int_0^t \text{SFR}(t') dt'}. \quad (6)$$

Integrating equations (4) and (5), and combining with equation (6), we can obtain the analytical solutions of the chemical evolution using appropriate initial conditions. In other words, both the gas-phase metallicity and the mean stellar metallicity solutions can be obtained. There are four different solutions corresponding to four special cases.

The first case includes both gas inflow and outflows, i.e., $\omega \neq 0$ and $\lambda \neq 0$, and $\alpha \neq -1$. The initial conditions are $M_{*,0} = 0$ and $M_{g,0} = M_g + (1 + \alpha)M_*$, and the solutions are

$$\begin{cases} Z_g = \frac{y}{\omega} \{1 - [1 + (1 + \alpha) \frac{M_*}{M_g}]^{-\beta}\}, \\ \langle Z_* \rangle = -\frac{y}{\omega(1 + \alpha)} \{[1 - \frac{1 + \alpha}{1 + \lambda} [1 + (1 + \alpha) \frac{M_*}{M_g}]^{-\beta}] \frac{M_g}{M_*} \\ - \frac{\omega}{1 + \lambda} [\frac{M_g}{M_*} + (1 + \alpha)]\}, \end{cases} \quad (7)$$

where $\beta = \frac{\omega}{1 + \alpha}$. We should emphasize that the values of λ and ω are conditional. Since the initial gas mass should not be less than zero, i.e., $M_{g,0} \geq 0$, the value of mass accretion factor is constrained to the range $\omega \leq \lambda + \frac{1}{1 - \mu}$, where μ is the gas fraction and defined as

$$\mu = \frac{M_g}{M_g + M_*}.$$

The second case is $\alpha = -1$. The initial conditions are $M_{*,0} = 0$ and $M_{g,0} = M_g = \text{const}$, and the corresponding solutions are

$$\begin{cases} Z_g = \frac{y}{\omega} (1 - e^{-\omega \frac{M_*}{M_g}}), \\ \langle Z_* \rangle = \frac{y}{\omega} [1 + \frac{M_g}{\omega M_*} (e^{-\omega \frac{M_*}{M_g}} - 1)]. \end{cases} \quad (8)$$

The third case is no gas inflow but with gas outflow, i.e., $\omega \neq 0$ and $\lambda = 0$. The initial conditions are $M_{*,0} = 0$ and $M_{g,0} = M_g + (1 + \lambda)M_*$, and the solutions are

$$\begin{cases} Z_g = \frac{y}{1 + \lambda} \ln[1 + (1 + \lambda) \frac{M_*}{M_g}], \\ \langle Z_* \rangle = \frac{y}{(1 + \lambda)^2} \{ (1 + \lambda) - \frac{M_g}{M_*} \ln[1 + (1 + \lambda) \frac{M_*}{M_g}] \}. \end{cases} \quad (9)$$

The last one is the closed-box model with neither gas inflows nor outflows, i.e., $\omega = 0$ and $\lambda = 0$, the initial conditions are $M_{*,0} = 0$ and $M_{g,0} = M_g + M_*$, and the solutions become

$$\begin{cases} Z_g = y \ln[1 + \frac{M_*}{M_g}], \\ \langle Z_* \rangle = y [1 - \frac{M_g}{M_*} \ln(1 + \frac{M_*}{M_g})]. \end{cases} \quad (10)$$

The above equations show that, given the two free parameters λ and ω , the gas-phase and stellar metallicity at time t can be calculated by the stellar-to-gas mass ratio at that moment. In order to illustrate this point clearly, Figure 1 displays the gas-phase metallicity (left) and the stellar metallicity (right) as a function of the stellar-to-gas mass ratio with different combinations of the parameters λ and ω . The lines with different colors correspond to different outflow loading factors (i.e., red $\lambda = 0$, blue $\lambda = 0.5$ and cyan $\lambda = 1.0$), while the different line-types are corresponding to different mass accretion factors (i.e., solid $\omega = 0$, dashed $\omega = 0.5$ and dotted $\omega = 1.0$). We should point out that the left panel of Figure 1 is similar to the Figure 1 of [Kudritzki et al. \(2015\)](#). Here we add the panel of stellar metallicity as a function of the stellar-to-gas mass ratio and simultaneously explore the gas-phase and stellar metallicity.

The left panel of Figure 1 shows that the closed-box model (the red-solid line) provides the upper limits of the gas-phase metallicity. Gas outflow removes part of metal content from the system and reduces the final gas-phase metallicity, while gas inflow slows down the ISM chemical enrichment by adding pristine gas. Unfortunately, since both the gas inflow and the gas outflows reduce the gas-phase metallicity, a degeneracy between parameters λ and ω exists in the stellar-to-gas mass range of $\log(M_*/M_g) = 0$ to $\log(M_*/M_g) = 1.4$, which makes it difficult to disentangle the

role of outflow and inflow from the observations of the gas-phase metallicity only.

On the other hand, the stellar component in the right panel of Figure 1 shows a different behavior for $-0.2 \leq \log(M_*/M_g) \leq 1.4$. For a given outflow loading factor λ , the mean stellar metallicity increases with the mass accretion factor ω , because large inflow factor means large fraction of star forms at late time and then having high metallicity. Based on the gas-to-stellar relation of [Peeples et al. \(2014, Eq.\(9\)\)](#) from ~ 260 star-forming galaxies, the typical range of the stellar-to-gas ratio is about $-0.07 \leq \log(M_*/M_g) \leq 1.13$ for star-forming galaxies with stellar mass $9.0 \leq \log(M_*/M_\odot) \leq 11.5$. Therefore, the observed stellar metallicity may help us to overcome the parameter degeneracy and serve as an important observable to constrain the SFHs of star-forming galaxies. In the following Sections, we choose M 101 as an example to demonstrate the importance of stellar metallicity in the chemical enrichment studies.

3 THE OBSERVATIONS

As described in Section 2, with our model, spatially resolved gas-phase and stellar metallicities can be calculated from the spatially resolved stellar-to-gas mass ratio. In this Section, we summarize the observed radial distribution of these properties for M 101, including the gas-phase metallicity, the stellar metallicity, the mass surface densities of ISM neutral and molecular hydrogen and the stellar mass surface density.

3.1 Stellar and gas mass surface densities

The stellar mass surface density (Σ_*) is derived from infrared (IR) surface photometry obtained with the 2MASS survey ([Jarrett et al. 2003](#)) using the K -band at $2.2\mu\text{m}$. The K -band surface brightness profile from [Muñoz-Mateos et al. \(2007\)](#) and the fixed K -band mass-to-light ratio, $Y_*^K = 0.5M_\odot/L_{\odot,K}$ (see [Leroy et al. 2008](#)), is adopted to calculate Σ_* .

The neutral hydrogen gas mass surface density (Σ_{HI}) of M 101 is obtained from Very Large Array (VLA) maps of the 21-cm hydrogen line as part of The HI Nearby Galaxy Survey (THINGS; [Walter et al. 2008](#)). The molecular hydrogen gas mass surface density (Σ_{H_2}) is derived by CO ($J = 2 - 1$) maps carried out by using the IRAM 30m as part of the HERA CO-Line Extragalactic Survey (HERACLES; [Leroy et al. 2009](#)). A factor of 1.36 has been included to account for the contribution of helium and heavier elements, and the reader is referred to [Schruba et al. \(2011\)](#) for more details about the conversion of emission (21-cm and CO) line into Σ_{HI} and Σ_{H_2} , respectively. The total gas mass surface density (Σ_{gas}) is defined as $\Sigma_{\text{gas}} = \Sigma_{\text{HI}} + \Sigma_{\text{H}_2}$.

3.2 Metallicity gradients

Since oxygen is the element most commonly measured and taken as a tracer for the total metal content, and because it is an element for which the IRA approximation is appropriate, we will use the oxygen abundance to represent the metallicity of M 101 and adopt the solar value as $12 + \log(\text{O}/\text{H})_\odot = 8.69$ ([Asplund et al. 2009](#)) throughout this work.

The radial distribution of gas-phase metallicity of HII regions in M 101 have been obtained in several works, notably [Kennicutt & Garnett \(1996\)](#), [Kennicutt et al. \(2003\)](#), [Bresolin \(2007\)](#), [Li et al. \(2013\)](#) and [Croxall et al. \(2016\)](#) and [Hu et al.](#)

(2018). The gas-phase metallicity from [Kennicutt & Garnett \(1996\)](#) and [Hu et al. \(2018\)](#) are calculated by using the theoretical calibration published by [Kobulnicky & Kewley \(2004, hereafter KK04\)](#), while those from [Kennicutt et al. \(2003\)](#), [Bresolin \(2007\)](#), [Li et al. \(2013\)](#) and [Croxall et al. \(2016\)](#) are derived by using the direct Te methods. Since the absolute gas-phase metallicity depends on the calibrations used, it is crucial to use the same metallicity calibration when using the observations to constrain the model. Te method is considered as the most reliable approach to determine the gas-phase metallicity ([Izotov et al. 2006](#)), and the gas-phase metallicity obtained from the direct Te method is systemically ~ 0.4 dex lower than that from the KK04 calibration ([Hu et al. 2018](#)). Consequently, we use the gas-phase metallicity data obtained from direct Te calibration to constrain the model. We also add the data based on the KK04 but subtract 0.4 dex to account for the systematic effect of this calibration.

The radial distribution of stellar metallicity for M 101 is derived by [Lin et al. \(2013\)](#), who fitted evolutionary population synthesis model ([Bruzual & Charlot 2003](#)) to a set of multi-band photometry images from ultraviolet, optical and infrared together with the 15 intermediate-band images observed in the Beijing-Arizona-Taiwan-Connecticut (BATC) filter system. The BATC photometric system covers the wavelength range of $3300 - 10000\text{\AA}$, and the bandwidths of the intermediate-band filters are about $200 - 300\text{\AA}$. The reader is referred to Table 1 in [Lin et al. \(2013\)](#) for more details about the effective wavelengths of the filters and some statistics of the stacked images. It should be pointed out that [Lin et al. \(2013\)](#) used a fixed metallicity when performing SED fitting for each pixel, that is, simple stellar populations of different ages have the same metallicity. Thus, the mean stellar metallicity they obtained inclines to a luminosity-weighted metallicity. The luminosity-weighted metallicity cannot be corrected to the mass-weighted metallicity by using the mass-to-light ratio in a specific band. Moreover, since the simple model we are using does not contain specific information of SFH, we are not able to convert a mass-weighted metallicity predicted by our model into a luminosity-weighted metallicity. We have to tolerate that this may add some uncertainties to our results. Fortunately, Figure 11 in [Lin et al. \(2013\)](#) shows that the disc of M 101 is dominated by intermediate-age stellar populations (~ 6 Gyr) and the age gradient is quite flat, which indicates the mass-to-light ratio may not vary significantly in the disc of M 101. It should also be noted that the stellar metallicity data in [Lin et al. \(2013\)](#) are obtained from multi-band photometry. Such a determination is generally very uncertain, and this is a challenge for star-forming galaxies. To use spectroscopic stellar metallicity to constrain the model would be much better, unfortunately, no such data are available for M 101.

The radial distribution of metallicity depends on the distance to M 101, and we note that the distance used in [Schruba et al. \(2011\)](#) is the same as the distances used by [Lin et al. \(2013\)](#), [Croxall et al. \(2016\)](#) and [Hu et al. \(2018\)](#), but different from those used in [Kennicutt & Garnett \(1996\)](#), [Kennicutt et al. \(2003\)](#), [Bresolin \(2007\)](#) and [Li et al. \(2013\)](#). Consequently, we have scaled all the metallicity distributions of M 101 to the distance used by [Schruba et al. \(2011\)](#), and the value of the distance to M 101 is taken from [Karachentsev et al. \(2004\)](#). The left panel of Figure 2 plots the observed radial distribution of gas-phase metallicity of HII regions in M 101 from different authors as different symbols, and the observed radial distribution of stellar metallicity data from [Lin et al. \(2013\)](#) is displayed in the right panel of Figure 2. It should be pointed out that, since the gas mass surface density taken from

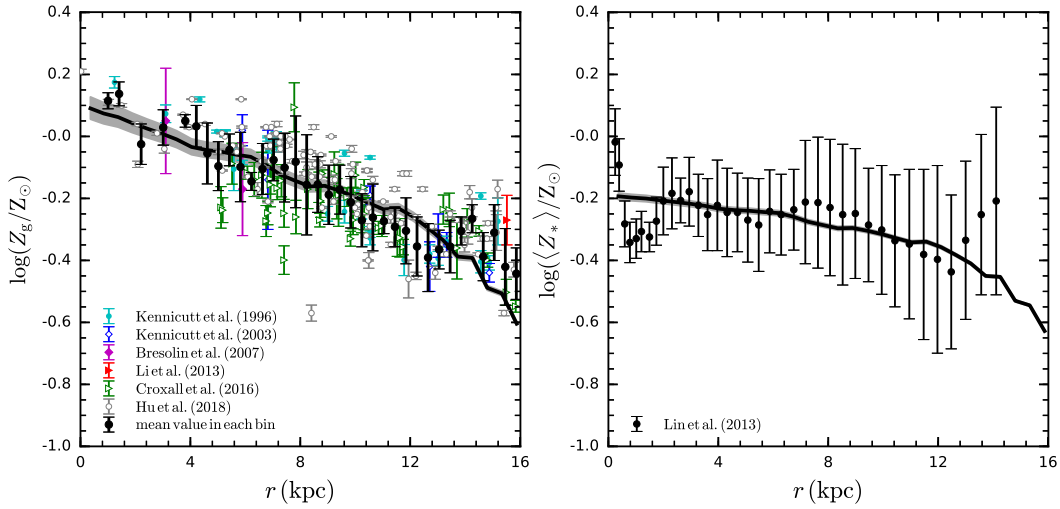


Figure 2. Comparison of model predicted metallicity with observations in M 101 (left: gas-phase; right: stars). *Left panel:* different symbols denote the observed gas-phase metallicity from different authors. The cyan solid and grey open cycles represent the gas-phase metallicity calculated by using the calibration of KK04, while the blue open diamonds, magenta solid diamonds, the red solid triangles and green open triangles are corresponding to the gas-phase metallicity derived by using the direct Te calibrations. Note that the KK04 calibration data are corrected to remove the discrepancies between Te and KK04 calibrations (see text). The black solid cycles display the mean values of observed gas-phase metallicity in each bin, and the error bars are the standard deviation of data in each bin. *Right panel:* the observed stellar metallicity data are shown as black solid cycles. The solid lines in both panels plot the best-fitting model predictions adopting $(\lambda = 1.137, \omega = 0.781)$, while the grey shaded area denote the model predictions adopting $(\lambda = 1.069, \omega = 0.689)$ and $(\lambda = 1.207, \omega = 0.869)$ with 1σ confidence level.

Schruba et al. (2011) goes only out to $r \sim 16$ kpc, we only adopt the observed gas-phase metallicity within the disc range $r \leq 16$ kpc.

The solid lines of Figure 2 are the predictions of the best-fitting model, and the grey shaded regions are the model predictions that enclose 1σ confidence level, which will be described in detail in the following Section.

4 RESULTS AND DISCUSSION

As has been described in Sections 2 and 3, with the observed radial distributions of the stellar mass, gas mass and metallicity in the disc of M 101 together with the metallicity yield y , we can determine the outflow loading factor λ and the mass accretion factor ω of the analytical chemical evolution model presented in Section 2. For a given galactic-centric radius r , we use the observed stellar-to-gas ratio at the present-day to calculate gas-phase and stellar metallicity based on the model solutions in Section 2. In other words, for each parameter combination of λ and ω , we generate a model library of radial metallicity profile for both gas-phase and stellar components. We use the classical χ^2 methodology to compare the model predictions with the corresponding observed data. Referring to the definition by Press et al. (1992, Eq.(15.1.5)), we adopt $\chi^2 = \sum_{i=1}^N \frac{(C_{\text{model},i} - C_{\text{obs},i})^2}{\sigma_i^2}$, where σ_i is the observed error and N is the number of observed data. The model that minimizes this reduced χ^2 is considered as the best-fitting model.

In order to ensure gas-phase and stellar metallicity have nearly the same weight, we divide the radial observed gas-phase metallicity data introduced above along the disc ($r \leq 16$ kpc) of M 101 into 36 bins, which is the same number as that of the stellar component. Then, we calculate the mean values of gas-phase metallicity in each bin and show them as big black solid cycles in the left panel of Figure 2, where the error bars represent the standard deviation of data in each bin. Since the error of some gas-phase metallicity

data are not known, following the approach of Press et al. (1992, Eq.(15.1.6)), we assume that all the observed metallicity data have the same standard deviation, $\sigma_i = \sigma$, and that the model does fit well, that is, we adopt the reduced χ^2 , $\chi^2_{\nu} = 1$, to fit the data. According to $\chi^2_{\nu} = \frac{\chi^2}{N-M}$, where $N-M$ is the number of degrees of freedom for fitting N data points with M parameters, we can get $\chi^2 = N-M$.

We separately calculate the values of χ^2 for gas-phase metallicity (χ^2_g), stellar metallicity (χ^2_*) and both gas-phase and stellar metallicity ($\chi^2_g + \chi^2_*$). The boundary conditions are adopted to be $0 \leq \lambda \leq 4.5$ and $0 \leq \omega \leq 4.5$, respectively. χ^2 contour maps are displayed in Figure 3. The left, the middle and the right panels separately plot χ^2_g , χ^2_* and $\chi^2_g + \chi^2_*$ contours. The minimum values of χ^2 are shown as red filled asterisks in these three panels of Figure 3. The solid lines display the isocontours of $\Delta\chi^2 = \chi^2 - \chi^2_{\min} = 2.3$ (blue), 6.17 (cyan) and 11.8 (brown) corresponding to 1σ (68.3%), 2σ (95.4%) and 3σ (99.73%) confidence levels. It should be emphasized that the oblique line traversing across the red asterisk in the middle panel arises from the constraint condition $\omega \leq \lambda + \frac{1}{1-\mu}$ in equation 7 as described in Section 2.

The left panel of Figure 3 indicates the degeneracy between parameters λ and ω , that is, the higher inflow rate and the lower outflow rate show similar χ^2 values as the lower inflow rate and the higher outflow rate. The physical reason is that gas-phase metallicity is diluted by the pristine gas inflow at a fixed radius, and the enriched outflow process takes a fraction of metals away from the disc at a fixed radius. Indeed, the large area of χ^2 contours in the left panel indicates that it is difficult to determine the model parameters only using the gas-phase metallicity. The corresponding values of the best parameter combinations are $\lambda = 1.768$ and $\omega = 0.338$. On the other hand, the middle panel of Figure 3 shows that stellar metallicity is more sensitive to λ than to ω . The best parameter combinations are $\lambda = 2.456$ and $\omega = 3.485$. The degeneracy in this case is weaker than the former case. Moreover, the

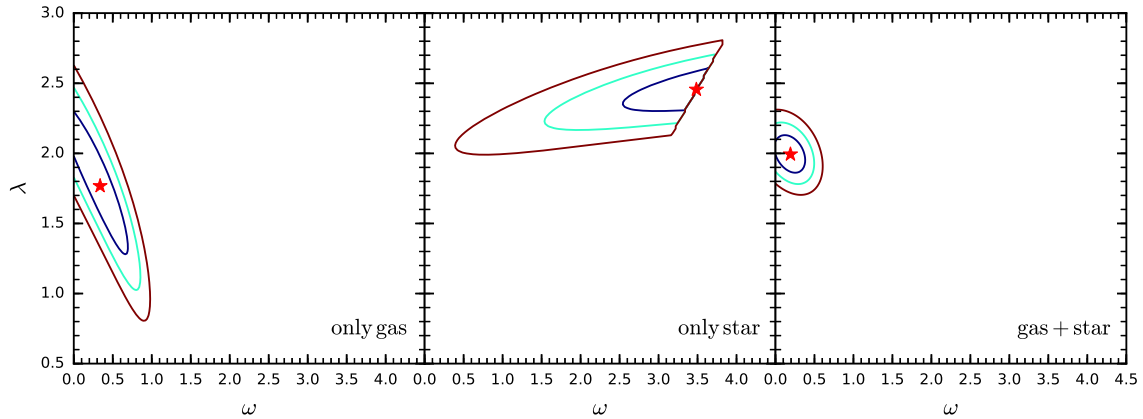


Figure 3. χ^2 contour maps for the outflow loading factor λ and the mass accretion ω determinations. Only gas-phase metallicity (left), only stellar metallicity (middle) and both gas-phase and stellar metallicity (right) are used to constrain the model. The red filled asterisk in each panel denotes the minimum value of χ^2 . The $\Delta\chi^2$ values adopted for these plots are 2.3 (blue), 6.17 (cyan) and 11.8 (brown), which are corresponding to 68.3%, 95.4% and 99.73% confidential levels, respectively.

direction of the degeneracies is different in two cases. In consequence, the combined fitting is most effective for the constraint of the parameters.

After using both gas-phase and stellar metallicity as constraints, the right panel shows that the reasonable range of model parameters is significantly reduced. The minimum value of χ^2 can be found at $\lambda = 1.994$ and $\omega = 0.192$. Furthermore, the degeneracy between ω and λ in the left panel is lifted, which implies that stellar metallicity may help us to determine the best combination of ω and λ . In other words, the observed stellar metallicity provides an additional constraint on the chemical enrichment history of M 101.

We name the model with $\lambda = 1.994^{+0.125}_{-0.136}$ and $\omega = 0.192^{+0.089}_{-0.088}$ as the best-fitting model of M 101. The best-fitting model predicted radial profiles of gas-phase and stellar metallicity are respectively shown as solid lines in the left and right panels of Figure 2. The grey shaded regions in both panels display the model results within 1σ confidence level, that is, $(\lambda = 1.906, \omega = 0.056)$ and $(\lambda = 2.083, \omega = 0.317)$. It should be emphasized that, although we do not take into account the radial variations of model parameters along the disc in this paper, a good agreement between the solid lines and the observed data indicates that the gas outflow rate ($\Psi = 1.418^{+0.089}_{-0.097} \times \text{SFR}$) and gas inflow rate ($\Phi = 0.136^{+0.063}_{-0.062} \times \text{SFR}$) may reasonably describe the fundamental physical processes regulating the formation and evolution of M 101.

Another point we should emphasize is that, the observed metallicity gradient of the gas-phase component is much steeper than that of stellar component. In other words, the difference between Z_g and $\langle Z_* \rangle$ (hereafter ΔZ) decreases with the increase of radius. Previous studies have shown that there exists a strong correlation between ΔZ and the mean age of stellar populations $\langle t \rangle$ in the sense that larger ΔZ corresponds to older mean stellar age. For further discussion, we refer the reader to Peng et al. (2015) and to Figure 5 of Ma et al. (2016). Our results indicate that the inner disc of M 101 has an older stellar population than the outer disc, which is consistent with the inside-out formation scenario of stellar discs.

Furthermore, we should discuss the influence of the stellar yield y on the determination of model parameters. It can be found from equation sets 7, 8, 9 and 10 in Section 2 that the stellar yield y is proportional to the resulted metallicity, thus the adopted y is expected to largely influence the resulting model parameters. Fig-

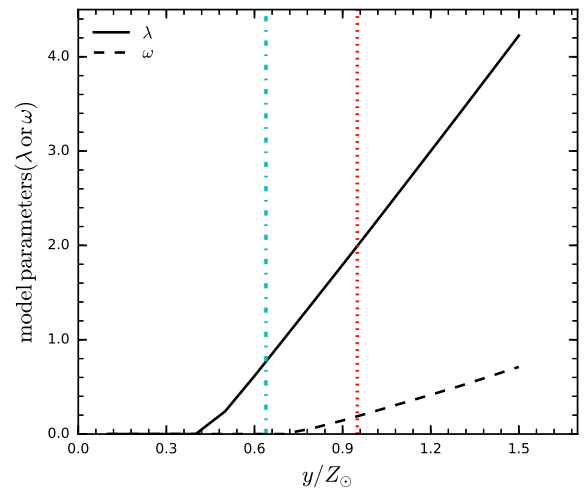


Figure 4. The model parameters λ and ω as a function of the yield y/Z_\odot . The solid and dashed lines are corresponding to λ and ω , respectively. The vertical red dotted line denotes the value of the yield adopted in this work, while the vertical cyan dash-dotted line marks the yield adopted in Kudritzki et al. (2015).

ure 4 plots the best-fitting model parameters λ and ω as a function of the yield y . The striking feature of Figure 4 is that the value of outflow parameter λ is very sensitive to the adopted yield y , since the main effect of gas outflow process is to take away part of newly synthesized metals and reduce the metallicity of the ISM. In fact, this is a common difficulty in studies of the chemical evolution of galaxies. Therefore, the absolute value of λ derived in this paper is not robust, and we can only estimate the relative probability of λ for given stellar yield.

Finally, we note that the best combination of λ and ω for M 101 derived by Kudritzki et al. (2015) is $\omega = 0.0$ and $\lambda = 0.98$, that is, $\Phi = 0$ and $\Psi = 0.98$ in units of SFR, who use the gas-phase metallicity to constrain the model. The smaller values of λ and ω for M 101 in Kudritzki et al. (2015) than ours (see both left and right panels of Figure 3) mainly due to the fact that they adopted a smaller stellar yield than ours.

5 SUMMARY

In this work, the radial distribution of gas-phase and stellar metallicity of star-forming galaxies is investigated by means of an analytical chemical evolution model. We find that the gas-phase and stellar metallicity can be derived by the ratio of stellar-to-gas mass surface densities. Through comparing the gas-phase metallicity with the stellar metallicity as a function of the stellar-to-gas mass ratios with models of different combinations gas inflow and outflow rates, it is shown that both gas inflow and outflows can reduce the gas-phase metallicity, but there exists degeneracy effect between ω and λ . On the other hand, stellar metallicity is more sensitive to λ than to ω , and this helps to reduce the degeneracy effect. The analytical chemical evolution model is applied to the nearby disc galaxy M 101. By means of the classical χ^2 methodology, ω and λ are better determined by simultaneously using gas-phase and stellar metallicity as the observed constraints, which further indicates that stellar metallicity is an important additional observable to constrain the SFH of star-forming galaxies. Our results also show that relatively strong gas outflows but weak inflows occurred on the disc of M 101 during its evolutionary history.

Recent IFU surveys provide large samples of data for star-forming galaxies which include spatially resolved information of observed stellar mass, gas mass, gas-phase metallicity and stellar metallicity. This will provide an opportunity for further tests our method. We plan to apply the analytical chemical evolution model to a large sample of star-forming galaxies to constrain the gas inflow and outflows during their evolutionary histories in our future work.

ACKNOWLEDGEMENTS

We thank the anonymous referee for thoughtful comments and insightful suggestions that greatly improved the quality of this paper. This work is supported by National Key R&D Program of China (No. 2019YFA0405501). Xiaoyu Kang and Fenghui Zhang are supported by the National Natural Science Foundation (NSF) of China (No. 11973081, 11573062, 11403092, 11390374, 11521303), the YIPACAS Foundation (No. 2012048), the Chinese Academy of Sciences (CAS, KJZD-EW-M06-01), the NSF of Yunnan Province (No. 2019FB006) and the Youth Project of Western Light of CAS. Ruixiang Chang is supported by the National NSF of China (No. 11373053, 11390373). Rolf Kudritzki acknowledges support by the Munich Excellence Cluster Origins Funded by the Deutsche Forschungsgemeinschaft (DFG, German Research Foundation) under the German Excellence Strategy EXC-2094 390783311.

DATA AVAILABILITY

The data underlying this article will be shared on reasonable request to the corresponding author.

REFERENCES

Asplund, M., Grevesse, N., Sauval, A. J., & Scott, P. 2009, *ARA&A*, 47, 481
 Belfiore, F., Maiolino, R., & Bothwell, M. 2016, *MNRAS*, 455, 1218
 Bouché, N., Dekel, A., Genzel, R., et al. 2010, *ApJ*, 718, 1001
 Bresolin, F. 2007, *ApJ*, 656, 186
 Bruzual, G. & Charlot, S. 2003, *MNRAS*, 344, 1000
 Bundy, K., Bershad, M. A., Law, D. R., et al. 2015, *ApJ*, 798, 7

Chang, R. X., Hou, J. L., Shu, C. G., & Fu, C. Q. 1999, *A&A*, 350, 38
 Chang, R. X., Hou, J. L., Shen, S. Y., & Shu, C. G. 2010, *ApJ*, 722, 380
 Croxall, K. V., Pogge, R. W., Berg, D. A., Skillman, E. D., & Moustakas, J. 2016, *ApJ*, 830, 4
 Esteban, C., Bresolin, F., García-Rojas, J., et al. 2020, *MNRAS*, 491, 2137
 Freedman, W. L., Madore, B. F., Gibson, B. K., et al. 2001, *ApJ*, 553, 47
 Hou, J. L., Prantzos, N., & Boissier, S. 2000, *A&A*, 362, 921
 Izotov, Y. I., Stasińska, G., Meynet, G., et al. 2006, *A&A*, 448, 955
 Jarrett, T. H., Chester, T., Cutri, R., et al. 2003, *AJ*, 125, 525
 Hu, N., Wang, E., Lin, Z., et al. 2018, *ApJ*, 854, 68
 Kang, X., Chang, R., Yin, J., et al. 2012, *MNRAS*, 426, 1455
 Kang, X., Zhang, F., Chang, R., Wang, L., & Cheng, L. 2016, *A&A*, 585, A20
 Kang, X., Zhang, F., & Chang, R. 2017, *MNRAS*, 469, 1636
 Karachentsev, I. D., Karachentseva, V. E., Huchtmeier, W. K., et al. 2004, *AJ*, 127, 2031.
 Kennicutt, R. C., Jr., & Garnett, D. R. 1996, *ApJ*, 456, 504
 Kennicutt, R. C., Jr., Bresolin, F., & Garnett, D. R. 2003, *ApJ*, 591, 801
 Kobulnicky, H. A., & Kewley, L. J. 2004, *ApJ*, 617, 240
 Kroupa, P., Tout, C. A., & Gilmore, G. 1993, *MNRAS*, 262, 545
 Kudritzki, R.-P., Ho, I.-T., Schruha, A., et al. 2015, *MNRAS*, 450, 342
 Leroy, A. K., Walter, F., Brinks, E., et al. 2008, *AJ*, 136, 2782
 Leroy, A. K., Walter, F., Bigiel, F., et al. 2009, *AJ*, 137, 4670
 Li, Y., Bresolin, F., & Kennicutt, R. C., Jr. 2013, *ApJ*, 766, 17
 Lian, J., Thomas, D., Maraston, C., et al. 2018a, *MNRAS*, 474, 1143
 Lian, J., Thomas, D., Maraston, C., et al. 2018b, *MNRAS*, 476, 3883
 Lilly, S. J., Carollo, C. M., Pipino, A., et al. 2013, *ApJ*, 772, 119
 Lin, L., Zou, H., Kong, X., et al. 2013, *ApJ*, 769, 127
 Ma, X., Hopkins, P. F., Faucher-Giguère, C.-A., et al. 2016, *MNRAS*, 456, 2140
 Matteucci, F. & Chiosi, C. 1983, *A&A*, 123, 121
 Matteucci, F., & Francois, P. 1989, *MNRAS*, 239, 885
 McCall, M. L., Rybski, P. M., & Shields, G. A. 1985, *ApJS*, 57, 1
 Mihos, J. C., Keating, K. M., Holley-Bockelmann, K., Pisano, D. J., & Kasim, N. E. 2012, *ApJ*, 761, 186
 Muñoz-Mateos, J. C., Gil de Paz, A., Boissier, S., et al. 2007, *ApJ*, 658, 1006
 Peebles, M. S., Werk, J. K., Tumlinson, J., et al. 2014, *ApJ*, 786, 54
 Peng, Y., Maiolino, R., & Cochrane, R. 2015, *Nature*, 521, 192
 Press, W. H., Teukolsky, S. A., Vetterling, W. T., & Flannery, B. P. 1992, Cambridge: University Press, [c1992, 2nd ed.,
 Recchi, S., Spitoni, E., Matteucci, F., & Lanfranchi, G. A. 2008, *A&A*, 489, 555
 Romano, D., Karakas, A. I., Tosi, M., et al. 2010, *A&A*, 522, A32
 Sánchez, S. F., Kennicutt, R. C., Gil de Paz, A., et al. 2012, *A&A*, 538, A8
 Sancisi, R., Fraternali, F., Oosterloo, T., & van der Hulst, T. 2008, *A&ARv*, 15, 189
 Schmidt, M. 1959, *ApJ*, 129, 243
 Schruha, A., Leroy, A. K., Walter, F., et al. 2011, *AJ*, 142, 37
 Searle, L. 1971, *ApJ*, 168, 327
 Silk, J. 2003, *MNRAS*, 343, 249
 Smith, H. E. 1975, *ApJ*, 199, 591
 Spitoni, E., Calura, F., Matteucci, F., & Recchi, S. 2010, *A&A*, 514, A73
 Spitoni, E., Vincenzo, F., & Matteucci, F. 2017, *A&A*, 599, A6
 Tinsley, B. M. 1980, *Fundamentals Cosmic Phys.*, 5, 287
 Vincenzo, F., Matteucci, F., Belfiore, F., et al. 2016, *MNRAS*, 455, 4183
 Waller, W. H., Bohlin, R. C., Cornett, R. H., et al. 1997, *ApJ*, 481, 169
 Walter, F., Brinks, E., de Blok, W. J. G., et al. 2008, *AJ*, 136, 2563
 Yabe, K., Ohta, K., Akiyama, M., et al. 2015, *ApJ*, 798, 45
 Zahid, H. J., Dima, G. I., Kudritzki, R.-P., et al. 2014, *ApJ*, 791, 130
 Zahid, H. J., Kudritzki, R.-P., Conroy, C. et al. 2017, *ApJ*, 847, 18

This paper has been typeset from a \LaTeX file prepared by the author.